ASSESSING FLUID-GAS EXPULSION GEOLOGY AND GAS HYDRATE DEPOSITS ACROSS THE GULF OF MEXICO WITH MULTICOMPONENT AND MULTIFREQUENCY SEISMIC DATA

Bob A. Hardage[1], Harry H. Roberts[2], Diana C. Sava[1], Paul E. Murray[1], Michael V. DeAngelo[1], Milo M. Backus[1], and Robert J. Graebner[1]

[1]Bureau of Economic Geology, The University of Texas at Austin
[2]Coastal Studies Institute, Louisiana State University

ABSTRACT

We used single-component, high-frequency (1–10 kHz), chirp-sonar data acquired with autonomous underwater vehicle (AUV) technology and multicomponent, low-frequency (10-150 Hz) seismic data acquired with a standard surface-based air gun source and 4-component ocean-bottom-cable (4C OBC) technology to study two fluid-gas expulsion sites across a portion of the Green Canyon area of the Gulf of Mexico (GOM). One expulsion site was in Green Canyon Block 204 (GC 204) near Genesis Field in Green Canyon Block 205 (GC 205), and the second was near Typhoon field, which produces from Green Canyon Block 237 (GC 237). We found that the lower-frequency OBC P-SV seismic images produced by our specialized 4C seismic data-processing concepts revealed features of near-seafloor geology with a spatial resolution equivalent to that of kHz-range AUV chirp-sonar data. We processed and interpreted more than 90 km of 2D4C OBC data extending across two expulsion features we selected for study. This paper describes the multicomponent, multifrequency seismic technology we used in this study and summarizes the near-seafloor geology defined by these technologies across these two expulsion features.

Keywords: seismic imaging, joint inversion, S-waves

GEOLOGIC FRAMEWORK

Our two study sites, GC 237 and GC 204, were located in the Green Canyon Lease area where both deep-water fields and oil and gas seeps are numerous (Fig. 1). Both sites are positioned on the flank of an intraslope basin containing a thick sedimentary sequence. Seismic profiles across our areas of interest show that major fluid-gas migration pathways, identified as acoustically amorphous zones, occur near the edges of shallow subsurface salt masses.

At the GC 237 site, the principal feature of interest appears as a nearly circular region having both high and low seafloor reflectivity, as determined from standard, towed-cable, 3D seismic data (Fig. 2). Manned submersible dives on this feature revealed highly variable seafloor conditions throughout the area. Two sites of fluidized mud extrusion were discovered. These extrusion sites corresponded to the low-reflectivity zones shown on Figure 2 where mud volcanoes have developed. One of these features was a spectacular mud volcano rising over 10 m above the surrounding seafloor. The outside of this feature was covered with white flow patterns resulting from barium-rich fluids precipitating barite down the mound flanks (Fig. 2A). Several active gas seeps were observed at the top and on the flanks of the mound. Sampling revealed the presence of gas hydrate beneath the surface sediments.

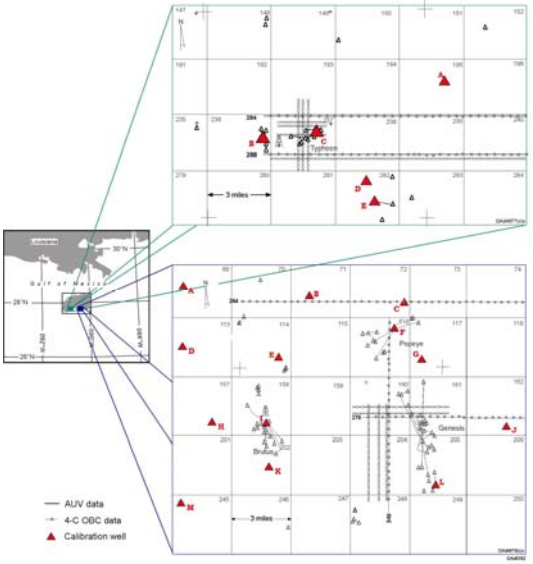

Figure 1. (Top) Database across the area of Typhoon field. A fluid-gas expulsion feature is located in GC 237. (Bottom) Database across the area of Genesis field. A fluid-gas expulsion feature is located in GC 204.

Surrounding this area of active fluidized sediment expulsion were zones of large reflection amplitude on the 3D-seismic seafloor reflectivity map. The high reflectivity of these areas was related to extensive regions of hard bottom composed of authigenic carbonates. Surrounding the large mud volcano, blocks of this carbonate were upturned (Fig. 2B). Around and between these carbonate blocks were living communities of tubeworms and mussels. These relationships persisted throughout the area. A region of brine seepage was observed along the western margin of this GC 237 feature.

Figure 3 illustrates the complexity of the surficial geology across GC 204 and surrounding lease blocks. This 3D-seismic seafloor reflectivity map defines several fluid-gas expulsion centers having low reflectivity and long mud flows trending down slope that exhibit much higher reflectivity. The mud flows originate from expulsion centers which are bathymetric highs and tend to have areas of bathymetrically complex seafloor surrounding them. Manned submersible observations indicate that the expulsion centers are still active, but at a level much lower than in the past when the long mud flows developed. Escaping gas and some evidence of localized fluidized sediment expulsion were observed. In towed-cable seismic profiles, the subsurface area beneath the cluster of expulsion sites is represented by an acoustically amorphous zone, assumed to be the principal fluid-gas migration pathway.

It is clear from the surficial geology of GC 204 that this area has experienced extrusions of large volumes of fluidized sediment. The timing for the major expulsion events that developed the long mud flow patterns seen in Figure 3 is unknown. The expulsion activity has obviously slowed to its present near-dormant state. On the high ground around the extrusion sites, the modern seafloor is irregular because of the presence of authigenic carbonate slabs, blocks, and low-relief mounds (Fig. 3A). These hard-bottom features contain clam and mussel shells that have been cemented by carbonates that are precipitated as a by-product of microbial oxidation of hydrocarbons. Surrounding the outcropping carbonates are densely populated shell beds composed of lucinid-vesycomyid clams and mussels. Although localized living mussels and clams are present, most of the shell beds do not represent living communities. The combination of carbonates and shell beds creates a large seafloor reflection coefficient, as represented by 3D seismic data (Fig. 3).

In contrast to the carbonate hardgrounds of the areas surrounding the extrusion sites, it is logical to assume that the fine-grained sediments that comprise the mud flows should have low reflectivity. However, Figure 3 indicates that these features actually have moderate to high acoustic amplitudes, similar to the areas surrounding the active expulsion sites. The reason for this acoustic response is the presence of numerous clam shells on the surface and

perhaps in the shallow subsurface of the flow (Fig. 3B). Lucinid-vesycomyid clams exploit hydrogen sulfide produced by microbial communities that metabolize hydrocarbons incorporated in the muds. Once the hydrogen sulfide is depleted, the clams die, leaving a bed of shells. With subsequent mud flows, new clam populations develop. It is reasonable to assume that the high reflectivity of some mud flows is caused by the accumulation of numerous stacks of these shell horizons.

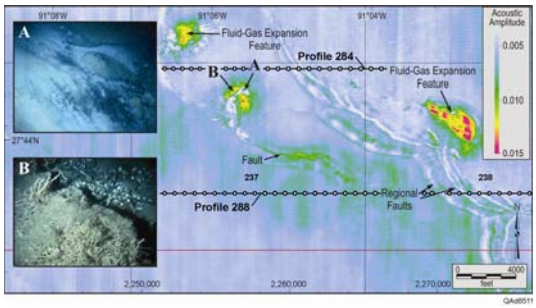

Figure 2. Seafloor reflectivity map constructed from towed-cable 3D seismic data shows a well-defined expulsion area in GC 237. Both high-reflectivity (red, yellow) and low-reflectivity (blue, white) areas are a part of this complex fluid-gas expulsion area. Low-reflectivity sites represent zones of fluidized sediment expulsion resulting in the creation of mud volcanoes. Extruded sediment and associated fluids have a high barium content. (A) This picture shows barite (white areas) on the flank of the mud volcano. (B) The high-reflectivity areas represent carbonate hardgrounds and slabs surrounded by active chemosynthetic communities (tube worms and mussels).

Our study focused on areas local to a fluid-gas expulsion feature located near Typhoon field (GC 237) and a second expulsion feature close to Genesis field (GC 205). Maps illustrating where AUV and OBC profiles traversed these two study sites are displayed as Figure 1. An important research finding was that low-frequency (10-150 Hz) OBC P-SV data resolved an interface that was sometimes less than 1 meter below the seafloor in the vicinity of these two deep-water expulsion features; whereas, high-frequency (1 – 10 kHz) AUV P-P data generated only 40 meters above the seafloor often did not image this horizon. Examples of these data behaviors are shown by horizons **A**, **B**, **C, D** labeled on the profiles displayed as Figure 4. As shown by these data, low-frequency, surface-source OBC P-SV data resolve some near-seafloor geologic features local to expulsion features (for example horizon **A**) better than do high-frequency, near-seafloor-source AUV P-P data, which is an important technology demonstration.

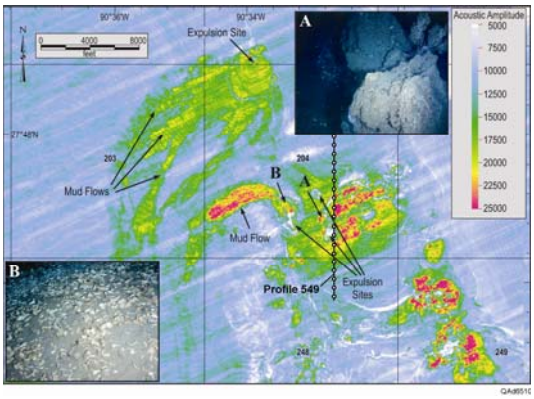

Figure 3. Within the region of GC 204, numerous expulsion centers and associated mud flows are defined by towed-cable, 3D-seismic, seafloor reflectivity data. Both the areas near the expulsion site and parts of the mud flows exhibit high reflectivity (red and yellow). (A) The high-amplitude areas surrounding the expulsion sites are zones of cemented seafloor with living mussel and clam beds. Large blocks of carbonate-cemented mussel shells and clam shells are typical of these areas. (B) Mud flows have high reflectivity because of dense seafloor accumulations of clam shells. Populations of lucinid-vesycomyid clams develop on new flows containing hydrocarbons. After exploiting hydrogen sulfide, a product of microbial oxidation of hydrocarbons, the community dies and leaves a carpet of shells on the surface. New flows provide another trophic resource for development of another community of clams. The large reflection amplitudes observed on towed-cable, 3D-seismic seafloor reflectivity data are assumed to be associated with multiple stratigraphic horizons of these clam shells.

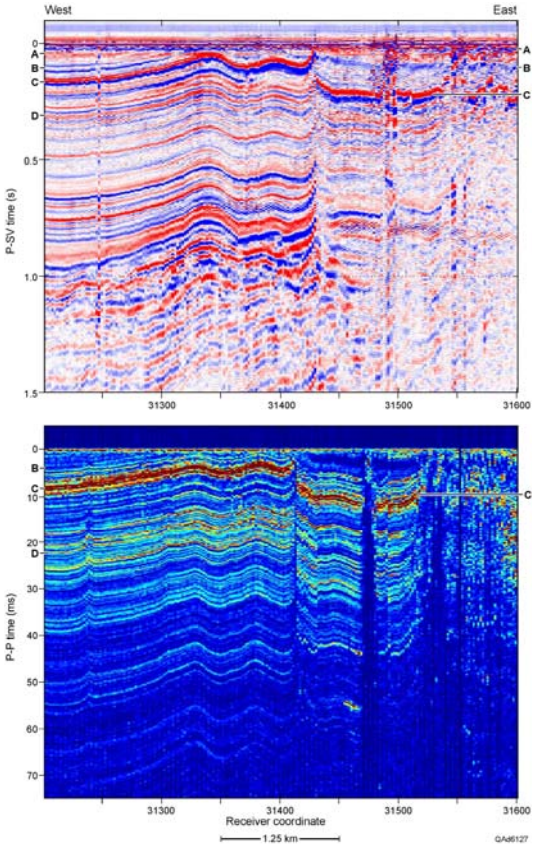

Figure 4. (Top) Interpreted P-SV image along OBC profile 276, Genesis Field (Fig. 1). (Bottom) Interpreted AUV P-P image. Depth-equivalent P-SV and P-P reflections are labeled **A** to **D**. Unit **A** is not imaged by the AUV data.

The reason for the superb resolution of OBC P-SV data is that the low values of V_S velocity in the shallowest seafloor strata, coupled with the fundamental equation,

$$\lambda_{SV} = V_S/f, \qquad (1)$$

that links wavelength (λ), velocity (V), and frequency (f), causes many SV wavelengths (λ_{SV}) to be less than 1 meter. The strategy we used to create the OBC P-SV image displayed in Figure 2 and the OBC P-P images shown later have been described by Backus and others (2006).

RAYTRACING TO DETERMINE LAYER VELOCITIES

Our first objective in interpreting the P-P and P-SV images that we produced along each OBC profile was to define which sub-seafloor P-SV reflection events occurring between the seafloor and the base of the hydrate stability zone (BHSZ) were depth-equivalent to selected P-P reflections existing across this same sub-seafloor depth interval. It is essential to define depth-equivalent P-P and P-SV reflections in order to create depth-equivalent V_P and V_S seismic interval velocities within sub-seafloor layers that have accuracies sufficient to make reliable estimates of hydrate concentration. We found that our interpreted horizons needed to be subjected to a rigorous numerical analysis to determine if each pair of "tentative" depth-equivalent P-P and P-SV reflections that we selected did indeed mark a depth-equivalent interface, or whether alternate reflection events needed to be used to establish depth equivalency. A major part of our research effort was the development and use of a raytracing procedure that:

1. created a system of sub-seafloor layers with defined thicknesses and with interpreter-specified V_P and V_S velocities,
2. calculated traveltimes along P-P and P-SV reflection raypaths through this velocity layering from a large number of sea-level air gun source stations to a common seafloor receiver station,
3. compared these calculated raytrace reflection times to actual times of the real-data P-P and P-SV reflections that were interpreted to be depth equivalent at that receiver station, and
4. adjusted layer thicknesses and V_P and V_S velocities until raytrace times and actual-data times for each pair of P-P and P-SV layer-interface reflections converged to acceptable agreement.

This sub-seafloor velocity-layer construction process was done at closely spaced seafloor receiver stations along each 2D OBC profile to build a continuous velocity layering of near-seafloor strata along the line of profile. Velocity Layer 1 started at the seafloor and extended to the shallowest interpretable P-P reflection.

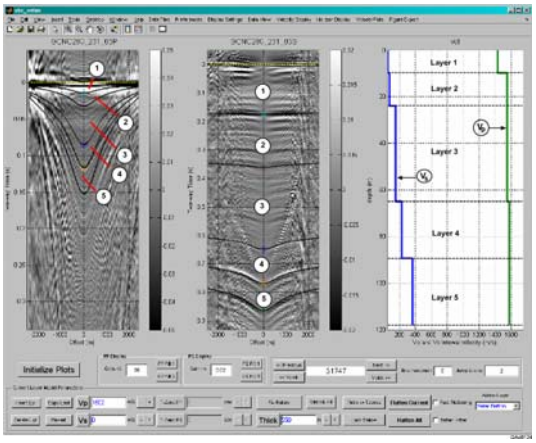

Figure 5. Establishing the velocity layering associated with depth-equivalent P-P and P-SV reflections recorded at a seafloor receiver station located on OBC profile 288, Typhoon Field (Fig. 1). Common-receiver-gathers were analyzed in the reduced-time domain, as shown here. The horizons positioned atop the P-P reflectivity (left) and the horizons drawn atop the P-SV reflections (center) are depth-equivalent. The depth equivalency between successive horizon pairs is confirmed by raytracing through the sub-seafloor layer thicknesses and V_P and V_S velocity profiles defined on the right. Sub-seafloor layer numbers **1** to **5** have been added to the data panels to help readers interpret the computer-screen display.

Velocity layers 2, 3, and 4 extended to successively deeper seafloor depths until a velocity layer N was created that extended deeper than the BHSZ boundary.

A computer screen display of a velocity raytrace analysis done at one seafloor receiver station is exhibited as Figure 5. This type of raytrace analysis was done using common-receiver gathers of P-P and P-SV reflectivity traces that were transformed to a reduced-time domain in which the time origin T = 0 at each source-offset coordinate was the direct-arrival time of the downgoing illuminating P wavefield at the seafloor receiver station. In the example in Figure 5, five depth-equivalent pairs of P-P and P-SV horizons are shown overlaying the P-P and P-SV reflectivity gathers. Reflection traveltimes are calculated downward to each layer interface from source stations extending 2.5 km to the left and right of the seafloor receiver (source-station interval = 50 m) and then upward to the seafloor receiver along reflected raypaths that pass through a user-defined sub-seafloor velocity layering (shown on the right). These raytrace times are then compared to each pair of "tentative" depth-equivalent P-P and P-SV reflections to determine if the reflections from each layer interface (right panel) are the horizons marked on the data displays (left and center panels). This raytracing approach to building a sub-seafloor layer model of V_P and V_S velocities produces estimates of interval velocities that can be quite accurate [1]. An alternate approach to determining high-resolution layer velocities to use to estimate hydrate concentration is described by Wood and others [2].

INTEGRATION OF RESISTIVITY, VELOCITY, AND SEISMIC DATA

We will use data at calibration wells B and C on OBC profile 264, approximately 10 km north of our AUV profiles at Genesis field (Fig. 1), to illustrate our joint-inversion technique for estimating hydrate concentration. We chose OBC profile 264 for this analysis because wells B and C are almost directly atop this profile, and the profile is reasonably close to the AUV profiles that traverse the expulsion site in Block GC204.

Data comparisons are shown at Well C first because of the geologic implications that result from data interpretations at this well location. First, the layer-velocity model built at Well C was stretched and squeezed to match the P-P and P-SV image-time axes at the well location, as shown in Figure 6. This

correlation process allows depth-based data to be compared against time-based seismic information. Inspection of the figure shows that each Earth-velocity layer correlates with a distinct seismic facies unit in both P-P image space and in P-SV image space. The V_P and V_S velocity profiles increase in unison from the seafloor to the base of Layer 3, and then the P and SV velocities change in opposing directions across the lower portion of the hydrate stability zone (Layers 4 and 5).

Three estimates of the base of the hydrate stability zone [BHSZ(90%), BHSZ(R), BHSZ(V)] are marked on each seismic profile. These horizons have the following meanings:

BHSZ(90%): The depth of the base of the hydrate stability zone for a natural gas chemistry having 90.4-percent methane which was calculated by Milkov and Sassen [3] for the hydrate system in Block GC185 near our study area using appropriate geothermal-gradient data.

BHSZ(R): The depth of a decrease in formation resistivity observed on the resistivity log acquired in calibration well C that is "close to" the depth of horizon BHSZ(90%) and that appears to be a logical choice for the base of the hydrate stability zone.

BHSZ(V): The depth of a decrease in V_P velocity defined by our raytrace-based velocity at well C that is "close to" the depth of horizon BHSZ(90%) and that appears to be a logical choice for the onset of free-gas trapped below the base of stable hydrate.

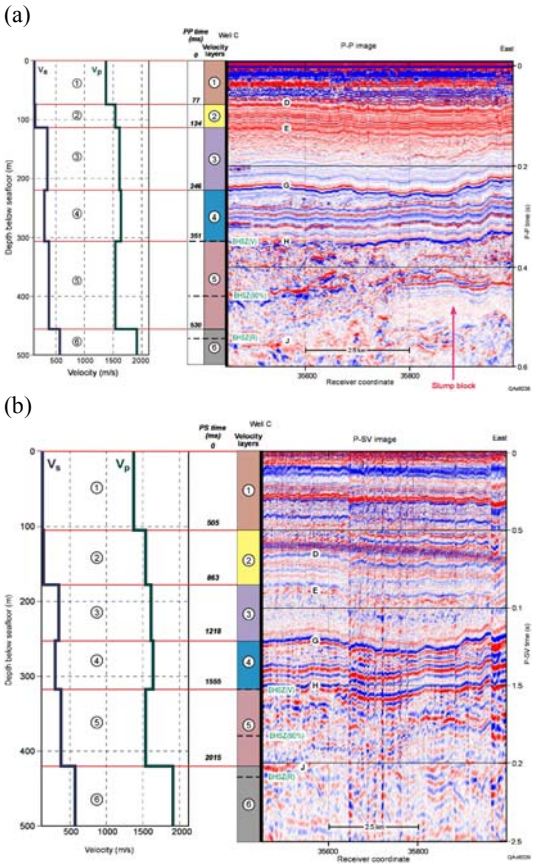

Figure 6. Integration of V_P and V_S velocity analysis at Well C with (a) P-P seismic data along OBC profile 264 (north of Genesis Field, Fig. 1) and (b) P-SV seismic data. Horizon BHSZ(R) is the base of the hydrate stability zone interpreted from the resistivity log (see Figure 7). Horizon BHSZ(V) is the adjusted position of the BHSZ based on velocity behavior.

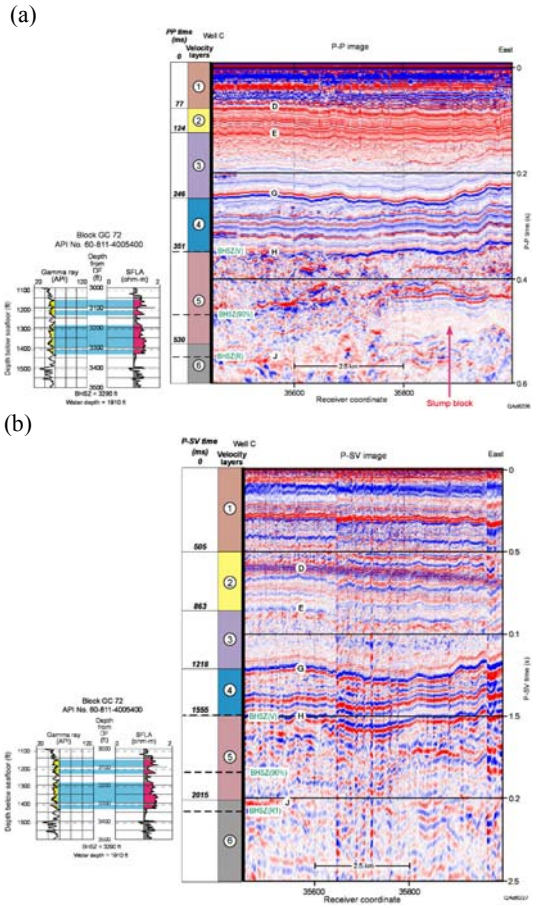

Figure 7. Integration of formation resistivity at Well C with (a) P-P seismic data along OBC profile 264 (north of Genesis Field, Fig. 1) and (b) P-SV seismic data. Horizon BHSZ(R) is the base of the hydrate stability zone interpreted from the resistivity log. Horizon BHSZ(V) is the adjusted position of the BHSZ based on velocity behavior (see Figure 6).

It is important to note that the V_P velocity profile at Well C (Fig. 6) exhibits an increasing trend in magnitude through Layer 4 and then undergoes a velocity reversal in Layer 5. It is also important to note that horizons BHSZ(90%) and BHSZ(R) at the base of Layer 5 are determined from the interpretation of resistivity logs and are independent of seismic-based V_P and V_S behavior.

The resistivity log from Well C is correlated with P-P and P-SV images traversing the well in Figure 7. At well C, all of the resistivity data associated with the interpreted hydrate stability zone are confined to velocity Layer 5. The position of the BHSZ(R) horizon shown on the figure is "interpreted" as the resistivity break at a depth of 1430 ft below the seafloor. A tentative dilemma presented by this data-correlation exercise is that formation resistivity increases in Layer 5, indicating increased hydrate content within the layer; whereas, the P-wave velocity decreases in Layer 5, which indicates decreased (or absent) hydrate content. We thus have opposing interpretations: resistivity data imply hydrate is present in Layer 5, but velocity data indicate hydrate is absent.

These observations led us to interpret the increased formation resistivity in velocity Layer 5 to be caused by free gas, not by hydrate. This adjusted interpretation of the resistivity log brings the resistivity data and velocity data at calibration well C into agreement because the decrease in V_P velocity in Layer 5 is also consistent with the presence of free gas. From this logic, we readjust the base of hydrate stability at Well C upward to depth BHSZ(V), the base of velocity Layer 4 where the reversal in V_P velocity begins. A valuable analysis of seismic velocities local to the base of hydrate stability has also been published by Yuan and others [4].

The integration of resistivity, velocity, and 4C seismic data at Well B is shown as Figures 8 and 9, using the information developed at Well C that resistivity-log behavior across velocity Layer 5 is caused by free gas, not by hydrate. Again, depth BHSZ(V), where there is a reversal in the magnitude of the seismic-based V_P interval velocity, appears to be the proper choice for the base of stable hydrate.

JOINT INVERSION OF RESISTIVITY AND VELOCITY

Joint-inversion estimates of hydrate concentration were made at one calibration well at Typhoon field (Well A, Fig. 1) and at one calibration well at Genesis field (Well

B, Fig. 1). The input data for these inversions were the resistivity log acquired in each calibration well and seismic-based V_P and V_S interval velocities determined from raytrace modeling local to each well. The rock physics theory used to relate V_P and V_S velocities to hydrate concentration is described by Sava and Hardage [5], [6]. The estimation of hydrate concentration at Well A, Typhoon field, that we determined using this theory is illustrated on Figure 10.

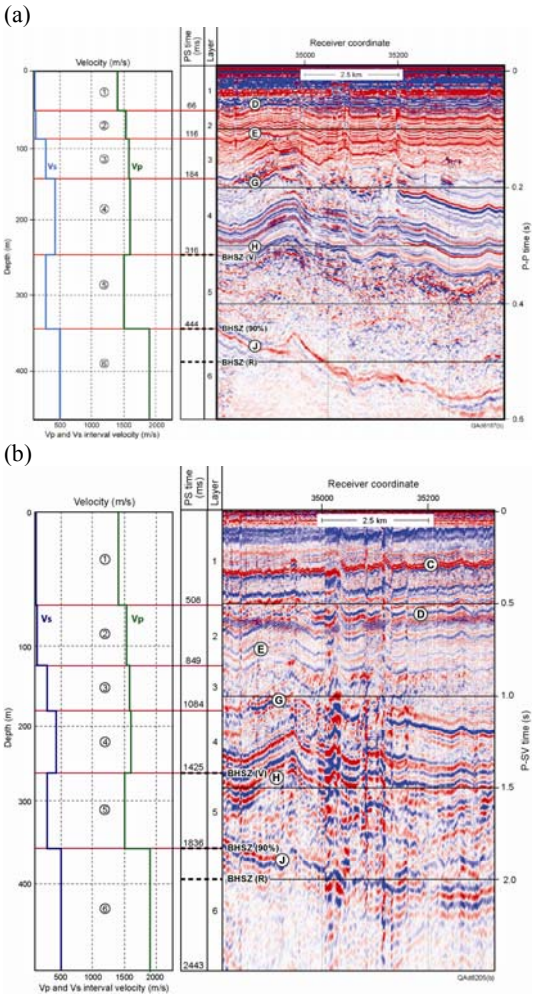

Figure 8. Integration of V_P and V_S velocity analysis at Well B with (a) P-P seismic data along OBC profile 264 (north of Genesis Field, Fig. 1) and (b) P-SV seismic data. Horizon BHSZ(R) is the base of the hydrate stability zone interpreted from the resistivity log (see Figure 9). Horizon BHSZ(V) is the adjusted position of the BHSZ based on velocity behavior.

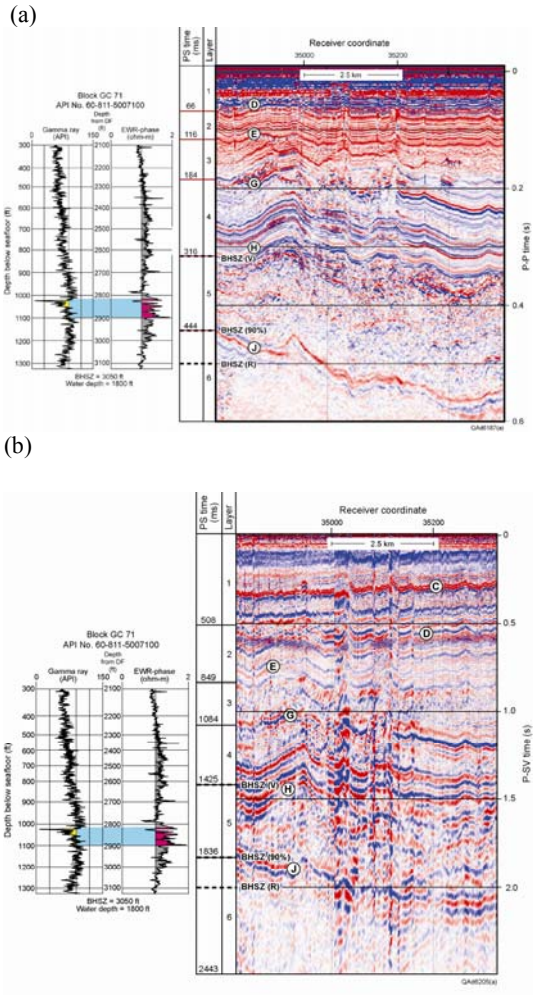

Figure 9. Integration of formation resistivity at Well B with (a) P-P seismic data along OBC profile 264 (north of Genesis Field, Fig. 1) and (b) P-SV seismic data. Horizon BHSZ(R) is the base of the hydrate stability zone interpreted from the resistivity log. Horizon BHSZ(V) is the adjusted position of the BHSZ based on velocity behavior (see Figure 8).

(a)

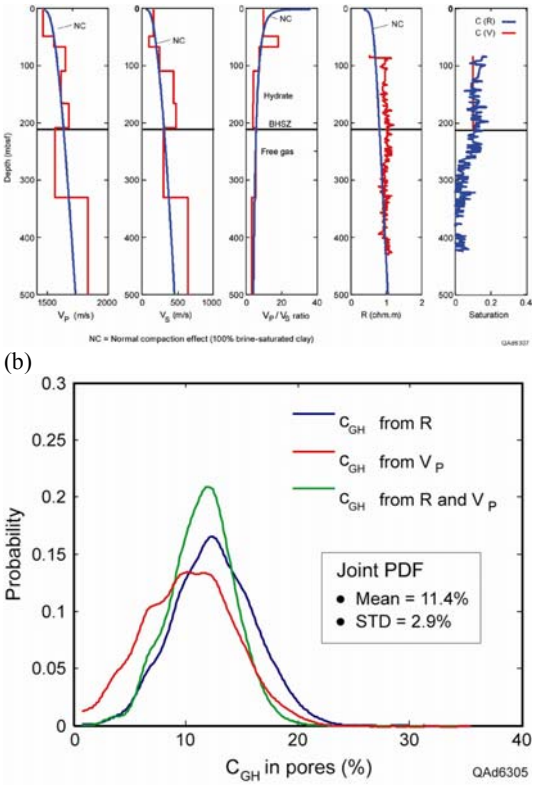

Figure 10. (a) Resistivity log, seismic-based V_P and V_S interval velocities, and their respective estimates of hydrate concentration at Well A, Typhoon Field (Fig. 1). The BHSZ boundary is defined as the top of the layer where V_P velocity exhibits a reversal in magnitude. The increase in resistivity below the BHSZ boundary is caused by free gas. (b) Joint inversion of resistivity and V_P velocity indicates hydrate occupies 11.4 percent of the pore space (mean value of the PDF). The estimation error is ±2.9 percent (standard deviation of the PDF).

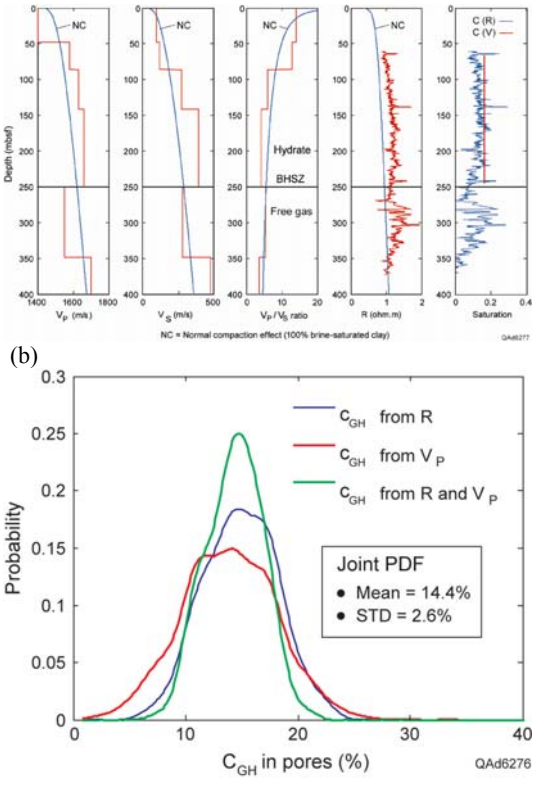

Figure 11. (a) Resistivity log, seismic-based V_P and V_S interval velocities, and their respective estimates of hydrate concentration at Well B, Genesis Field (Fig. 1). The BHSZ boundary is defined as the top of the layer where V_P velocity exhibits a reversal in magnitude. The increase in resistivity below the BHSZ boundary is caused by free gas. (b) Joint inversion of resistivity and V_P velocity indicates hydrate occupies 14.4 percent of the pore space (mean value of the PDF). The estimation error is ±2.9 percent (standard deviation of the PDF).

The function labeled NC on the data panels of this figure defines the effect of normal compaction on the specific rock property that is illustrated. This normal-compaction effect is calculated for a mixture of 95-percent clay and 5-percent quartz grains that are 100-percent brine saturated. The mineralogy fractions and depth-based porosity profile used to calculate this normal compaction curve were determined from data extracted from local seafloor core analyses and geotechnical reports provided by lease block operators. Depth intervals

above the BHSZ boundary where both velocity and resistivity have values greater than those associated with normal compaction are assumed to be zones of hydrate concentration. Using this normal-compaction behavior as a constraint for our joint inversion, the mean value of the probability distribution function (PDF) in Figure 8b indicates that hydrate occupies more than 11-percent of the pore space in the local vicinity of Well A. Results obtained at Well B, Genesis field, where hydrate is estimated to occupy a little more than 14-percent of the pore space, are exhibited as Figure 11.

The sediment-hydrate morphology that we used in this rock-physics modeling to account for the effect of hydrate concentration on seismic velocity assumed that the hydrate was "load-bearing." Our rock-physics theory also allows "floating, pore-filling" and "layered" hydrate-sediment morphologies to be used when appropriate [5], [6]. Calculations of V_P and V_S for seismic wave propagation in an unconsolidated, high-porosity, near-zero-effective-pressure medium such as exists near a deep-water seafloor agree with laboratory measurements of these velocities made by Yun and others [7] in similar media. Our rock-physics theory follows much of the logic of Helgerud and others [8] with the exception that we use Walton's theory [9] to describe shear modulus and stress. Our use of multiple data measurements (velocity and resistivity) in a joint inversion to estimate hydrate concentration is an approach also proposed by Zillmer [10].

2D PROFILES OF VELOCITY LAYERING

After performing joint inversions such as those illustrated in Figures 10 and 11, we determined an optimal suite of PDFs describing the statistical behavior of all mineral, brine, and hydrate properties (bulk modulus, shear modulus, density, coordination number) that were needed to relate hydrate concentration to seismic-based V_P velocity at OBC line coordinates between calibration wells. The input data for this velocity-based hydrate estimation were 2D profiles of V_P layer velocities determined by raytrace analysis of common-receiver gathers (see Fig. 5). These raytrace analyses were done at intervals of 10 receiver stations (250 meters) along each OBC profile. Examples of the 2D V_P and V_S velocity-layer models that we created along OBC profile 549 are exhibited as Figure 12.

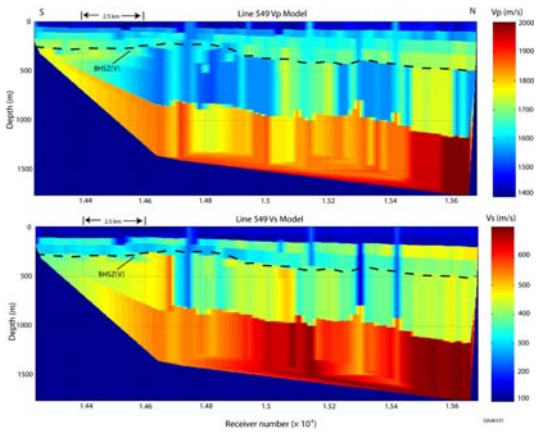

Figure 12. 2D V_P and V_S velocity models calculated along OBC profile 549, Genesis Field (Fig. 1) by raytrace analysis. The BHSZ(V) boundary is the dash line marking the top of the layer where V_P velocity has a reversal in magnitude. The layer model is depth adjusted so that the seafloor is shown as a flat datum at a depth coordinate of zero.

2D PROFILES OF HYDRATE CONCENTRATION

Relationships between V_P velocity and hydrate concentration developed at calibration wells were applied to the V_P velocity layer models constructed along each OBC profile we analyzed. The inversion results for the velocity layering along profile 549 (Fig. 12) are displayed as Figure 13.

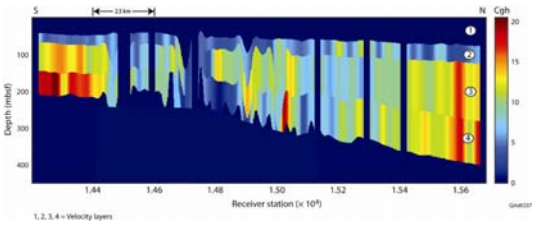

Figure 13. Hydrate concentrations estimated along OBC profile 549, Genesis Field (Fig. 1). The units are "percent of pore space occupied by hydrate". The seafloor is adjusted to a flat datum at a depth coordinate of zero.

CONCLUSIONS

We used 4C OBC seismic data and AUV chirp-sonar data to study near-seafloor geology near deep-water, fluid-gas expulsion features and to estimate hydrate concentrations in strata spanned by the hydrate stability zone local to these expulsion sites. Our research demonstrated that:

1. P-P and P-SV images made from 4C OBC seismic data yield higher-resolution definitions of near-seafloor geology than do high-frequency AUV data.
2. By utilizing raytrace procedures, high-resolution models of sub-seafloor layering of V_P and V_S velocities can be created at any selected seafloor-receiver station.
3. In high-porosity, unconsolidated, hydrate-bearing sediments, rock physics models that relate seismic velocities to hydrate concentration must be developed for several sediment-hydrate morphologies and combined with rock physics concepts that relate hydrate concentration to formation resistivity.
4. Probability distribution functions should be used to describe all variables that are used to estimate hydrate concentration.
5. A joint inversion of resistivity and velocity data is an optimal approach for estimating hydrate concentration within hydrate-bearing sediment.

We found that hydrate is pervasive across the two expulsion sites we studied at Typhoon and Genesis Fields, and that in some units, hydrate concentrations can be more than 30-percent of the available pore space of the host sediment. We discovered that a free-gas layer immediately underlies the base of the hydrate stability zone across each expulsion site area. This free-gas zone is revealed by a reduction in V_P velocity determined by our raytrace modeling technique. The amount of free gas in this zone was not estimated, but we expect the zone has a gas saturation of only a few percentage points. This free-gas zone was not obviously different from hydrate-bearing zones when examining resistivity logs available across our two study sites, and the increased resistivity related to this free-gas layer can be confused with a resistivity increase caused by hydrate. Interpreting the thickness of the hydrate stability zone from resistivity logs alone could lead to an overestimation of the thickness of the hydrate stability zone and of the amount of hydrate that is present near deep-water expulsion features.

Acknowledgments: *Our research was funded by the U.S. Department of Energy through contract DE-FC26-05NT42667 and by the Minerals Management Service through Cooperative Agreement 1435-01-02-CA-39076. WesternGeco provided the near-seafloor 4C OBC seismic data that we used in this study.*

REFERENCES

[1] Backus MM, Murray PE, Hardage BA, Graebner J. *High-resolution multicomponent seismic imaging of deepwater gas-hydrate systems*. The Leading Edge 2006; 25:578-596.

[2] Wood WT, Stoffa PL, Shipley TH. *Quantitative detection of methane hydrate through high-resolution seismic velocity*

analysis. J. Geophys. Res. 1994; 99:9681-9695.
[3] Milkov AV, Sassen R.. *Estimate of gas hydrate resource, northwestern Gulf of Mexico continental slope.* Marine Geology 2001;179:71-83.
[4] Yuan TS, Hyndman GD, Spence GD, Desmons B., *Seismic velocity increase and deep-sea gas hydrate concentration above a bottom-simulating reflector on the northern Cascadia continental slope.* J. Geophys. Res. 1996; 101:13655-13671.
[5] Sava D, Hardage B. *Rock physics characterization of hydrate-bearing deepwater sediments*. The Leading Edge 2006; 25:616-619.
[6] Sava D, Hardage B. *Rock-physics models for gas-hydrate systems associated with marine sediments*. In: Collett T, Johnson A, Knapp C, Boswell R, editors, Natural Gas Hydrates: Energy Resource Potential and Associated Geologic Hazards. AAPG Special Publication, 2008.
[7] Yun TS, Francisca FM, Santamarina JC, Ruppel C. *Compressional and shear wave velocities in uncemented sediment containing gas hydrate.* Geophys. Res. Lett. 2005; 32:L10609-L10613.
[8] Helgerud MB, Dvorkin J, Nur, A, Sakai, A, Collett, T. *Elastic-wave velocity in marine sediments with gas hydrates—effective medium modeling.* Geophys. Res. Lett. 1999; 26, 2021-2024.
[9] Walton K. *The effective elastic moduli of a random packing of spheres.* J. Mech. Phys. Solids 1987; 35:213-226.
[10] Zillmer M. *A method for determining gas-hydrate or free-gas saturation of porous media from seismic measurements.* Geophysics, 2006; 71:N21-N32, 10.1190/1.2192910.